

Mass and energy balance calculations for an artificial ice reservoir (Icestupa)

Suryanarayanan Balasubramanian^{1,*}, Martin Hoelzle¹, Michael Lehning²,

Sonam Wangchuk³, Johannes Oerlemans⁴ and Felix Keller⁵

¹ University of Fribourg, Fribourg, Switzerland

² WSL Institute for Snow and Avalanche Research, Davos, Switzerland

³ Himalayan Institute of Alternatives Ladakh, Leh, India

⁴ Institute for Marine and Atmospheric Research, Utrecht University, Utrecht, The Netherlands

⁵ Academia Engiadina, Samedan, Switzerland

Correspondence*:

Suryanarayanan Balasubramanian

suryanarayanan.balasubramanian@unifr.ch

2 ABSTRACT

Artificial Ice Reservoirs (AIR) have been successful in storing water during winter and releasing the water during spring and summer. This has made them a reliable fresh water resource for irrigation in dry environments. Several AIRs have been built but studies of their water storage capacity and efficiency are scarce. This study attempts to model a cone-shaped AIR popularly called Icestupa. Important processes involved in the development and temporal evolution of an Icestupa are calculated by a physically-based model using equations governing the heat transfer, vapour diffusion and transport of water that undergoes phase changes. These processes were quantified using meteorological data in conjunction with fountain spray information (mass input of an Icestupa) to estimate the quantity of frozen, melted, evaporated and runoff water at a location called 'Eispalast' in Fribourg, Switzerland. At this measurement site, an Icestupa was built for model validation purposes. The model was further tested by performing sensitivity and uncertainty study showing that the most sensitive parameters are the ice emissivity and the temperature threshold used to determine precipitation phase. Model calculations estimate that the Schwarzsee Icestupa stored about 8% of the total water sprayed as ice. In addition, we found that reducing nozzle diameter of the fountain to 3 mm increases the storage efficiency up to 93% without compromising on the storage duration.

Keywords: ictestupa, mass balance, water storage, climate change adaptation, geoengineering

1 INTRODUCTION

Seasonal snow cover, glaciers and permafrost are expected to change their water storage capacity due to climate change with major consequences for downriver water supply (Immerzeel et al., 2019). The challenges brought about by these changes are especially important for dry mountain environments such as in Central Asia or the Andes, which directly rely on the seasonal meltwater for their farming and drinking needs (Hoelzle et al., 2019; Apel et al., 2018; Buytaert et al., 2017; Chen et al., 2016; Unger-Shayesteh



Figure 1. Icestupa in Ladakh, India on March 2017 was 24 m tall and contained around 3.7 million litres of water. Picture Credits: Lobzang Dadul

25 et al., 2013). Some villages in Ladakh, India have already been forced to relocate due to glacial retreat and
26 the corresponding loss of their main fresh water resources (Grossman, 2015).

27 AIRs have been considered to be a feasible way to adapt to these changes (Hock et al., 2019; Nüsser
28 et al., 2019b). An artificial ice reservoir is a human-made ice structure typically constructed during the
29 cold winter months and designed to slowly release freshwater during the warm and dry spring and summer
30 months. The main purpose of AIR is irrigation. Therefore, AIRs are designed to store water in the form of
31 ice as long into the summer as possible. The energy required to construct an AIR is usually derived from
32 the gravitational head of the source water body. Some are constructed horizontally by freezing water using
33 a series of checkdams and others are built vertically by spraying water through fountain systems (Nüsser
34 et al., 2019a). The latter are colloquially referred to as Icestupas and are the subject of this study.

35 Since their invention in 2013 (Wangchuk, 2014), Icestupas have gained widespread publicity in the region
36 of Ladakh, Northern India since they require very little infrastructure, skills and energy to be constructed
37 in comparison to other water storage technologies. Compared to other AIR geometries, Icestupas (Fig.
38 1) can be built at lower altitudes and last much longer into the summer than other types of ice structures
39 (Wangchuk, 2014).

40 A typical Icestupa just requires a pipeline attached to a vertically mounted metal pipe with a fountain
41 nozzle for construction. Water source is usually a high altitude lake or glacial stream. Due to the altitude
42 difference between the pipeline input and fountain output, water ejects from the fountain nozzle as droplets
43 that eventually lose their latent heat to the atmosphere and accumulate as ice around the metal pipe.
44 The fountain nozzle is raised through addition of further pipes as and when significant ice accumulates.
45 Typically, a dome of branches is constructed around the metal pipe so that such pipe extensions can be
46 done from within this dome. During the winter, the fountain is manually activated between sunset and
47 sunrise. Threads, tree branches and fishing nets are used to guide and accelerate the ice formation.

48 If AIR are to become a viable water resource management tool, it is crucial to be able to propose suitable
49 construction sites, and to identify and minimize water losses. However, to date, no reliable estimates exist
50 about the amount of sprayed water that is necessary to create them and the meltwater they provide (Nüsser
51 et al., 2019a). Rough estimates of Icestupa meltwater in Ladakh suggest that the water loss during the

52 construction process is considerable (see Appendix 8.1). A complete set of measurements of the water
 53 storage and energy balance are required to understand the cause of the water losses better and increase the
 54 construction efficiency.

55 In this paper, we aim to develop a physically-based model of a vertical AIR (or Icestupa) that can quantify
 56 their storage efficiency using existing weather and water usage information. Mass and energy balance
 57 equations were used to estimate the quantity of water frozen, melted, evaporated and runoff. Sensitivity
 58 and uncertainty analysis were performed to identify the most critical parameters and the variance caused
 59 by them. For validation, we created an Icestupa at an accessible site (called Eispalast) near Schwarzsee in
 60 the Canton of Fribourg, Switzerland, allowing easy maintenance and control of the measurements. Due
 61 to the low altitude of the site with relatively high winter temperatures, only a small Icestupa could be
 62 established during winter 2018/19 for providing us with model validation data. Our model and validation
 63 experiments provide first steps towards evaluating the effectiveness of a vertical AIR for irrigation and
 64 finally we outline some preliminary guidelines for consideration when a construction of an Icestupa for
 65 water storage is envisaged.

2 STUDY SITE

66 The Eispalast site in the Schwarzsee region lies at 967 m a.s.l. In the winter (Oct-Apr), mean daily
 67 maximum and minimum air temperatures vary between 14 to -4 °C. Clear skies are rare, averaging around
 68 7 days, and precipitation amounts average 155 mm per month during winter (Meteoblue, 2020). The site
 69 was situated adjacent to a stream resulting in high humidity values across the study period. Within the
 70 Eispalast site, 1.8 m in radius enclosure was constructed for the experiment. An automatic weather station
 71 (AWS) was set in place adjacent to the wooden boundary as shown in Fig. 2. The fountain used for spraying
 72 water had a nozzle diameter of 5 mm and a height of 1.35 m, and was placed in the centre of the wooden
 73 enclosure. The water was transferred from a spring water source at 1267 m a.s.l. by pipeline and flowed
 74 via a flowmeter and an air escape valve to the nozzle, where it was sprinkled with a spray radius of around
 75 1.7 m. The air escape valve was installed to avoid errors in the flow measurements due to air bubbles. In
 76 addition, a webcam guaranteed a continuous survey of the site during the construction of the Icestupa.

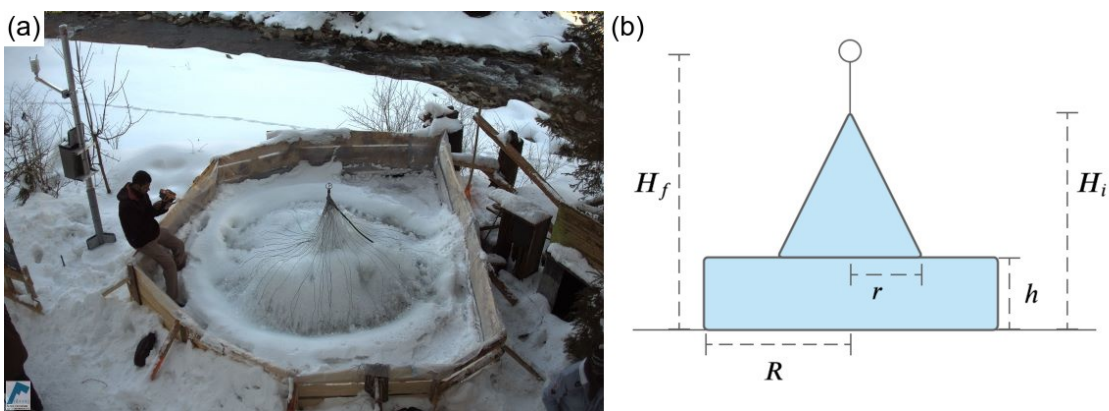


Figure 2. (a) The ice structure during the first validation measurement as seen on the webcam image of 14th Feb. (b) The corresponding cross section of the Schwarzsee ice structure with the field estimates of r , R , h , H_i , H_f used to determine the Icestupa volume is shown on the right.

77 2.1 Construction

78 From 30th January to 18th March 2019 the Icestupa was constructed through the fountain spray, which
 79 was manually switched on if measured air temperature was below -5 °C after sunset and was switched
 80 off as soon as the ice was exposed to daylight or temperatures were above 0 °C. The water spray of the
 81 fountain was initially adjusted so that most of the water droplets land within the wooden boundary zone.
 82 The ice formation was guided by adding a metal framework at the ice structure base after the first night of
 83 operation. Several cotton threads were tied between the ice structure base and fountain pole for accelerating
 84 and further guiding the ice formation process.

85 2.2 Measurements and Data

86 The Schwarzsee AWS was located at 967 m a.s.l. It was in operation from 30th January to 18th March
 87 2019. Measurements comprise air temperature, relative humidity, water flow, wind speed and direction.
 88 All these measurements were stored as 5 minute means. Precipitation data was derived from the Plaffeien
 89 AWS (IDAWEB, 2019) located 8.8 km away from the measurement site at an altitude of 1042 m a.s.l.

90 ERA5 reanalysis dataset (Copernicus Climate Change Service (C3S), 2017) was used to obtain the rest of
 91 the meteorological parameters. It has a horizontal resolution of approximately 30 km (Hersbach et al., 2020).
 92 Direct and diffuse shortwave radiation were derived from ERA5 surface solar radiation downwards and
 93 total sky direct solar radiation parameter. Total cloud cover parameter of ERA5 represented the cloudiness
 94 index. The hourly ERA5 data and the 10 minute Plaffeien AWS data were linearly interpolated to the 5
 95 minute data frequency of the Schwarzsee AWS.

96 Due to a power failure, all data from the Schwarzsee AWS was lost between 27th February 15:20 2019 to
 97 2nd March 15:00 2019. Consequently, the amount of missing data in the dataset was around 7%. During
 98 heavy snowfall events, the ultrasonic wind sensor was blocked and recorded zero values. To fill such
 99 errors and data gaps, we used the ERA5 reanalysis dataset as it was better correlated with the associated
 100 parameters in Schwarzsee compared to Plaffeien dataset. Namely, the 2m temperature parameter correlated
 101 ($r^2 =$) with air temperature, surface pressure parameter correlated ($r^2 =$) with air pressure and 10m wind
 102 speed parameter (derived from horizontal and vertical components) correlated ($r^2 =$) with wind speed.
 103 Near-surface humidity is not archived directly in ERA datasets, but from near-surface (2m from the surface)
 104 temperature (T_{ERA5}) and dew point temperature (Tw_{ERA5}) one can calculate relative humidity(RH) at
 105 2m as follows:

$$RH = 100 \cdot \frac{e_{sat}(Tw_{ERA5})}{e_{sat}(T_{ERA5})} \quad (1)$$

106 where the saturation vapour pressure function e_{sat} is expressed with the Teten's formula (Tetens, 1930):

$$e_{sat}(T) = a_1 \cdot e^{(a_3 \cdot \frac{T}{(T+273.16-a_4)})} \quad (2)$$

107 with T in °C and the parameters set for saturation over water ($a_1 = 611.21$ Pa, $a_3 = 17.502$ and $a_4 = 32.19$
 108 K) according to Buck (1981). Zero wind speed values were recorded whenever snow accumulated on the
 109 ultrasonic wind sensor. So all null values were replaced using the ERA5 dataset.

110 The ERA5 grid point chosen (Latitude 46° 38' 24" N, Longitude 7° 14' 24" E) for the Schwarzsee site
 111 was around 9 km away from the actual site. So all the ERA5 variables were fitted with the Schwarzsee
 112 dataset via linear regressions. Through this modified ERA5 dataset, we were also able to further extend the
 113 Schwarzsee dataset and allow the model to run beyond 18th March 2019. Precipitation was filled as null
 114 values beyond 18th March 2019.

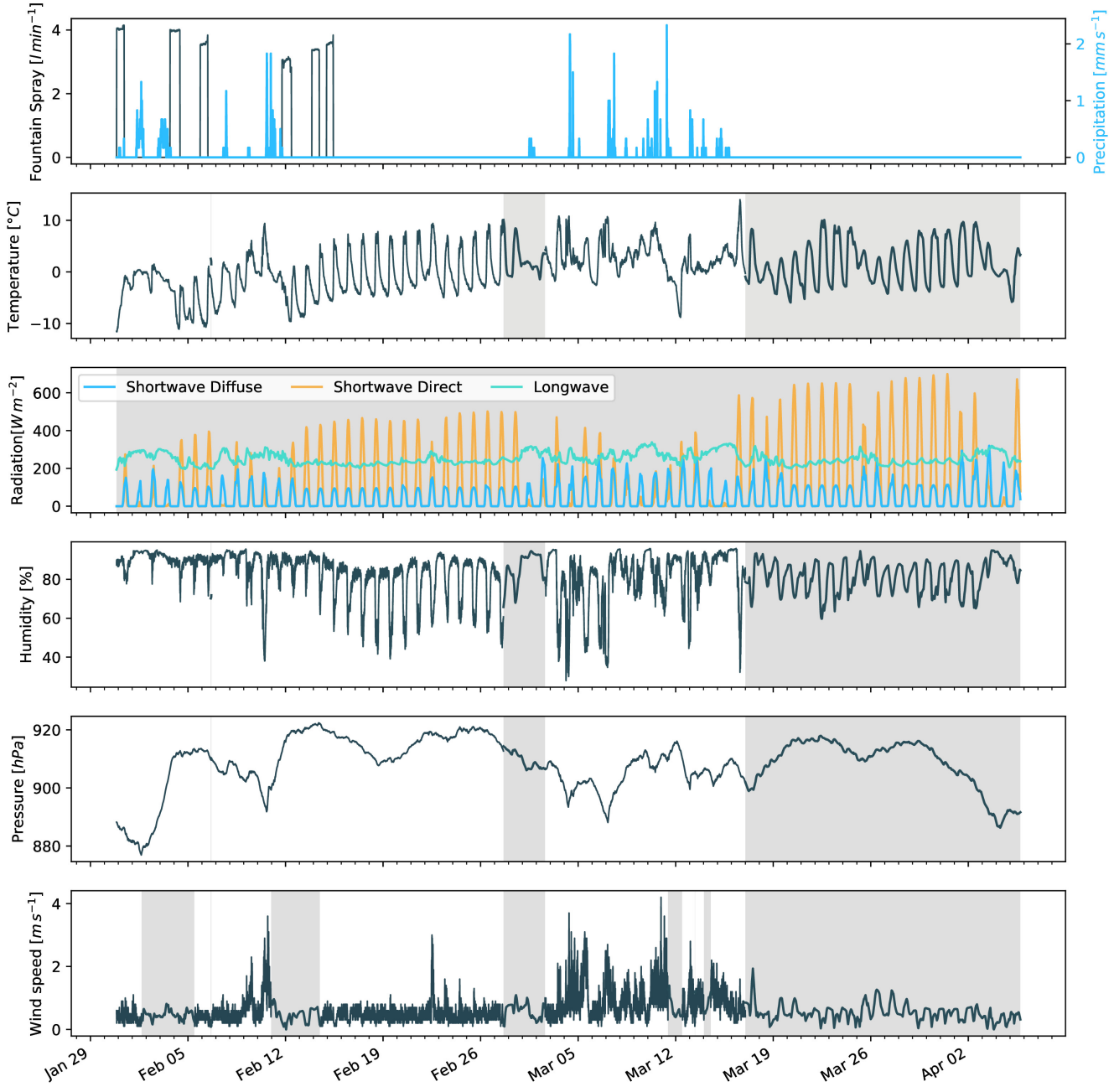


Figure 3. Measurements at the AWS of Schwarzsee were used as main model input data in 5 minute frequency. Plaffeien AWS provided the precipitation data. Incoming shortwave and longwave radiation were obtained from ERA5 reanalysis dataset. Several data gaps and errors were also filled from the ERA5 dataset (shaded regions).

115 2.2.1 Field Measurements for validation

116 The volume was determined by decomposing the ice structure into a cylinder (length $2R$ and height h)
 117 and a cone (radius r and height $(H_i - h)$) through the following equation:

$$V = \pi \cdot R^2 \cdot h + 1/3 \cdot \pi \cdot r^2 \cdot (H_i - h) \quad (3)$$

118 Manual measurements were performed at the end of the freezing period on 14th February 16:00 2019
 119 (only one more fountain run was possible after this date) to estimate r, R, h, H_i, H_f (see Fig. 2 for the
 120 different geometry components):

$$0.55 \leq r \leq 1m ; 1.1 \leq R \leq 1.2m ; 0.1 \leq h \leq 0.2m ; 0.6 \leq H_i \leq 0.8m ; 1.3 \leq H_f \leq 1.4m$$

121 The ranges of the variables show its variance across different compass orientations. Correspondingly, the
 122 volume range estimated for the first validation point was $0.857 \pm 0.186 m^3$ on 14th February 16:00 2019.

123 The second validation point corresponds to the end of the melting process on 10th March 18:00 2019.
 124 Based on the webcam imagery and manual measurement, a thin layer of ice with an observed thickness
 125 between 0.01 to 0.06 m could be quantified. This results in the volume range for the second validation to
 126 be $0.13 \pm 0.09 m^3$ on 11th March 2019

127 In reality, the Schwarzsee ice structure was more cylindrical until a height of 0.2 m and conical afterwards
 128 until a height of 0.6 m with a radius of 1.18 m. However, we assume a conical shape of this ice structure in
 129 order to apply the modelling strategy described below.

3 MODEL SETUP

130 The model (implemented in python) consists of three parts calculating a) the geometric evolution of the
 131 Icestupa, b) the energy balance and c) the mass balance as shown schematically in Fig. 4. A bulk energy
 132 and mass balance model is used to calculate the amounts of ice, liquid water, water vapour and runoff water
 133 of the Icestupa every 5 minutes. The equations used henceforth display model time step superscript only if
 134 it is different from the current time step.

3.1 Icestupa geometric evolution

136 Radius r_{ice} and height h_{ice} define the dimensions of the Icestupa assuming its geometry to be a cone as
 137 shown in Fig. 5. The surface area A exposed to the atmosphere and volume V are:

$$A = \pi \cdot r_{ice} \cdot \sqrt{r_{ice}^2 + h_{ice}^2} \quad (4)$$

$$V = \pi/3 \cdot r_{ice}^2 \cdot h_{ice} \quad (5)$$

138 With the mass of the Icestupa M_{ice} , its current volume can also be expressed as:

$$V = M_{ice}/\rho_{ice} \quad (6)$$

139 where ρ_{ice} is the density of ice ($917 kg m^{-3}$). The model of the Icestupa is initialised with a thickness
 140 of Δx (defined in 3.2) and a circular area of radius r_F . The constant r_F represents the mean spray radius
 141 of the fountain. This fountain spray radius is determined by modelling the projectile motion of the water
 142 droplets. Using mass conservation the droplet speed v_F can be determined from the spray rate d_F and the
 143 diameter dia_F of the nozzle as follows:

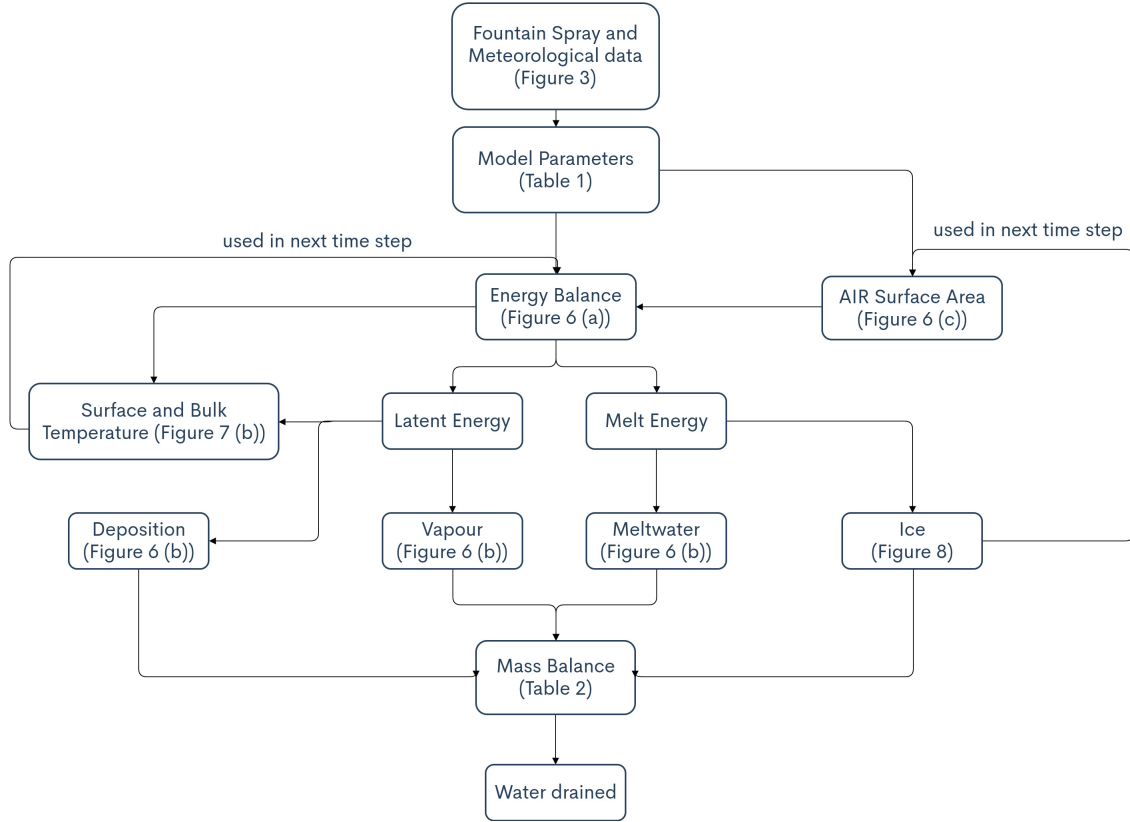


Figure 4. Model schematic showing the algorithm used in the model at every time step. Further details about these variables can be found in the associated tables and figures.

$$v_F = \frac{d_F}{\pi \cdot dia_F^2 / 4} \quad (7)$$

144 Afterwards, we assume that the water droplets move with an air friction free projectile motion from
 145 the fountain nozzle with a height h_F to the ice/ground surface. The resulting spray radius r_F was then
 146 determined from the projectile motion equation as follows:

$$r_F = \frac{v_F \cdot \cos\theta_F (v_F \cdot \sin\theta_F + \sqrt{(v_F \cdot \sin\theta_F)^2 + 2 \cdot g \cdot h_F})}{g} \quad (8)$$

147 where $g = 9.8ms^{-2}$ is the acceleration due to gravity and $\theta_F = 45^\circ$ is the angle of launch.

148 During subsequent time steps, the dimensions of the Icestupa evolve assuming a uniform ice formation
 149 and decay across its surface area with an invariant slope $s_{cone} = \frac{h_{ice}}{r_{ice}}$ as shown in Fig. 5. During these time
 150 steps, the volume is parameterised using Eqn. 5 as:

$$V = \pi/3 \cdot r_{ice}^3 \cdot s_{cone} \quad (9)$$

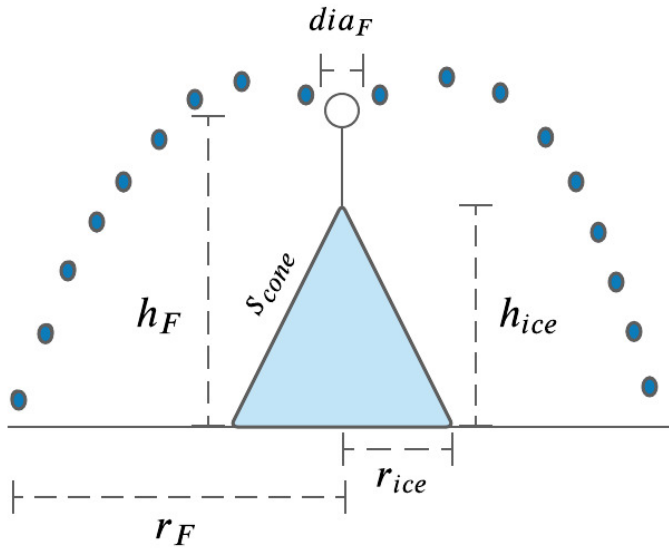


Figure 5. Shape and fountain parameters of the Schwarzsee Icestupa. r_{ice} is the radius, h_{ice} is the height and s_{cone} is the slope of the ice cone. r_F is the spray radius, h_F is the height and dia_F is the nozzle diameter of the fountain.

151 However, the Icestupa cannot outgrow the maximum range of the water droplets ($(r_{ice})_{max} = r_F$).
 152 Combining equations 5, 6 and 9, the geometric evolution of the Icestupa at each time step i can be
 153 determined by considering the following rules:

$$(r_{ice}, h_{ice}) = \begin{cases} (r_F, \Delta x) & \text{if } i = 0 \\ (r_{ice}^{i-1}, \frac{3 \cdot M_{ice}}{\pi \cdot \rho_{ice} \cdot (r_{ice}^{i-1})^2}) & \text{if } r_{ice}^{i-1} \geq r_F \text{ and } \Delta M_{ice} > 0 \text{ where } \Delta M_{ice} = M_{ice}^{i-1} - M_{ice}^{i-2} \\ (\frac{3 \cdot M_{ice}}{\pi \cdot \rho_{ice} \cdot s_{cone}})^{1/3} \cdot (1, s_{cone}) & \text{otherwise} \end{cases} \quad (10)$$

154 3.2 Energy Balance

155 The energy balance equation for the Icestupa is formulated as follows:

$$q_{net} = q_{SW} + q_{LW} + q_L + q_S + q_F + q_G \quad (11)$$

156 where q_{net} is the net energy flux in $[W m^{-2}]$; q_{SW} is the net shortwave radiation; q_{LW} is the net longwave
 157 radiation; q_L and q_S are the turbulent latent and sensible heat fluxes. q_F represents the heat exchange
 158 created due to the additional water and ice boundary present during fountain on time steps. q_G represents
 159 ground heat flux between Icestupa surface and Icestupa interior. Energy transferred in the direction of the
 160 ice surface is always denoted as positive and away as negative.

161 Equation 11 is usually referred to as the energy budget for “the surface”, but practically it must apply to a
 162 surface layer of ice with a finite thickness Δx . The energy flux acts upon the Icestupa surface layer which
 163 has an upper and a lower boundary defined by the atmosphere and the ice body of the Icestupa, respectively.
 164 The parameter selection for Δx is based on the following two arguments: (a) the ice thickness Δx should

165 be small enough to represent the daily surface temperature variations and (b) Δx should be large enough
 166 for these temperature variations to not reach the bottom of the surface layer. Therefore, we introduced a 5
 167 mm thick ice surface layer, over which the energy balance is calculated. A sensitivity analysis was later
 168 performed to understand the influence of this factor. Here, we define the surface temperature T_{ice} to be
 169 the modelled average temperature of the Icestupa surface layer and the energy flux q_{net} is assumed to act
 170 uniformly across the Icestupa area A .

171 3.2.1 Net Shortwave Radiation q_{SW}

172 The net shortwave radiation q_{SW} is computed as follows:

$$q_{SW} = (1 - \alpha) \cdot (SW_{direct} \cdot f_{cone} + SW_{diffuse}) \quad (12)$$

173 where SW_{direct} and $SW_{diffuse}$ are the ERA5 direct and diffuse short wave radiation, α is the modelled
 174 albedo and f_{cone} is the area fraction of the ice structure exposed to the direct shortwave radiation.

175 We model the albedo using a scheme described in Oerlemans and Knap (1998). The scheme records the
 176 decay of albedo with time after fresh snow is deposited on the surface. δt records the number of time steps
 177 after the last snowfall event. After snowfall, albedo changes over a time step, δt , as

$$\alpha = \alpha_{ice} + (\alpha_{snow} - \alpha_{ice}) \cdot e^{(-\delta t)/\tau} \quad (13)$$

178 where α_{ice} is the bare ice albedo value and τ is a decay rate, which determines how fast the albedo of the
 179 ageing snow reaches this value. The decay rate τ is assumed to have a base value of 10 days similar to
 180 values obtained by Schmidt et al. (2017) for wet surfaces and its maximal value is set based on observations
 181 by Oerlemans and Knap (1998) as shown in Table 1. Furthermore, the albedo α varies depending on the
 182 water source that formed the current Icestupa surface. Correspondingly, the albedo is reset to the value
 183 of bare ice albedo if the fountain is spraying water onto the current ice surface and to the value of fresh
 184 snow albedo if a snowfall event occurred. Snowfall events are assumed if the air temperature is below
 185 $T_{rain} = 1^{\circ}C$.

186 The area fraction f_{cone} of the ice structure exposed to the direct shortwave radiation depends on the
 187 shape considered. This factor is derived by calculating the area influenced by the vertical and horizontal
 188 components of the direct solar radiation. For a conical shape, half of the total curved surface is exposed to
 189 the vertical component of the direct shortwave radiation and the projected triangle of the curved surface
 190 is exposed to the horizontal component of the direct shortwave radiation. The solar elevation angle θ_{sun}
 191 used is modelled using the parametrisation proposed by Woolf (1968). Accordingly, f_{cone} is determined as
 192 follows:

$$f_{cone} = \frac{(0.5 \cdot r_{ice} \cdot h_{ice}) \cdot \cos\theta_{sun} + (\pi \cdot r_{ice}^2 / 2) \cdot \sin\theta_{sun}}{\pi \cdot r_{ice} \cdot (r_{ice}^2 + h_{ice}^2)^{1/2}} \quad (14)$$

193 The measured diffuse shortwave radiation is assumed to impact the conical Icestupa surface uniformly.

194 3.2.2 Net Longwave Radiation q_{LW}

195 The net longwave radiation q_{LW} , for which there were no direct measurements available at Schwarzsee,
 196 is determined as follows:

$$q_{LW} = LW_{in} - \sigma \cdot \epsilon_{ice} \cdot (T_{ice} + 273.15)^4 \quad (15)$$

197 where T_a represents the measured air temperature, T_{ice} is the modelled surface temperature, both
 198 temperatures are given in $^{\circ}\text{C}$, $\sigma = 5.67 \cdot 10^8 \text{ J m}^{-2} \text{ s}^{-1} \text{ K}^{-4}$ is the Stefan-Boltzmann constant, LW_{in}
 199 denotes the incoming longwave radiation derived from the ERA5 dataset and ϵ_{ice} is the corresponding
 200 emissivity value for the Icestupa surface (see Table 1).

201 3.2.3 Turbulent sensible q_S and latent q_L heat fluxes

202 The turbulent sensible q_S and latent heat q_L fluxes are computed with the following expressions proposed
 203 by Garratt (1992):

$$q_S = c_a \cdot \rho_a \cdot p_a / p_{0,a} \cdot \frac{\kappa^2 \cdot v_a \cdot (T_a - T_{ice})}{(\ln \frac{h_{AWS}}{z_{ice}})^2} \quad (16)$$

$$q_L = \begin{cases} 0.623 \cdot L_s \cdot \rho_a / p_{0,a} \cdot \frac{\kappa^2 \cdot v_a (p_{v,a} - p_{v,ice})}{(\ln \frac{h_{AWS}}{z_{ice}})^2} & \text{if } \Delta M_F = 0 \\ 0 & \text{if } \Delta M_F > 0 \text{ where } \Delta M_F = M_F^i - M_F^{i-1} \end{cases} \quad (17)$$

204 where h_{AWS} is the measurement height above the ground surface of the AWS (in m), v_a is the wind
 205 speed in $[m \text{ s}^{-1}]$ and M_F denotes fountain water spray mass in $[kg]$. c_a is the specific heat of air at
 206 constant pressure ($1010 \text{ J kg}^{-1} \text{ K}^{-1}$), ρ_a is the air density at standard sea level (1.29 kg m^{-3}), $p_{0,a}$ is the air
 207 pressure at standard sea level (1013 hPa), κ is the von Karman constant (0.4), L_s is the heat of sublimation
 208 (2848 kJ kg^{-1}) and z_{ice} (1.7 mm) denotes the roughness length of ice (momentum and scalar). The vapor
 209 pressures over air ($p_{v,a}$) and ice ($p_{v,ice}$) was obtained using the following formulation given in WMO
 210 (2018):

$$\begin{aligned} p_{v,a} &= 6.107 \cdot 10^{(7.5 \cdot T_a / (T_a + 237.3))} \\ p_{v,ice} &= (1.0016 + 3.15 \cdot 10^{-6} \cdot p_a - 0.074 \cdot p_a^{-1}) \cdot (6.112 \cdot e^{(22.46 \cdot T_{ice} / (T_{ice} + 272.62))}) \end{aligned} \quad (18)$$

211 where p_a is the measured air pressure in $[hPa]$.

212 3.2.4 Fountain water heat flux q_F

213 The total energy flux is further influenced through the heat flux caused by the water that was additionally
 214 added to the surface of the Icestupa during the time the fountain was running. We take this interaction
 215 between the fountain water and the ice surface into account by assuming that the ice surface temperature
 216 stays constantly at 0°C during time steps when the fountain is active. This process can be divided into two
 217 simultaneous steps: (a) the water temperature T_{water} is cooled to 0°C and (b) the ice surface temperature is
 218 warmed to 0°C . Process (a) transfers hereby the necessary energy for process (b) throughout the fountain
 219 runtime. We further assume that this process is instantaneous, i.e. the ice temperature is immediately set
 220 to 0°C within just one time step Δt when the fountain is switched on. Thus, the heat flux caused by the
 221 fountain water is calculated as follows:

$$q_F = \begin{cases} 0 & \text{if } \Delta M_F = 0 \\ \frac{\Delta M_F \cdot c_{water} \cdot T_{water}}{\Delta t \cdot A} + \frac{\rho_{ice} \cdot \Delta x \cdot c_{ice} \cdot T_{ice}}{\Delta t} & \text{if } \Delta M_F > 0 \end{cases} \quad (19)$$

222 with c_{ice} as the specific heat of ice.

223 3.2.5 Bulk Icestupa heat flux q_G

224 The bulk Icestupa heat flux q_G corresponds to the ground heat flux in normal soils and is caused by
225 the temperature gradient between the surface layer and the ice body. It is expressed by using the heat
226 conduction equation as follows:

$$q_G = k_{ice} \cdot (T_{bulk} - T_{ice}) / l_{ice} \quad (20)$$

227 where k_{ice} is the thermal conductivity of ice in $[W m^{-1} K^{-1}]$, T_{bulk} is the mean temperature of the ice
228 body within the Icestupa and l_{ice} is the average distance of any point in the surface to any other point in the
229 ice body. T_{bulk} is initialised as $0^\circ C$ and later determined from Eqn. 20 as follows:

$$T_{bulk} = T_{bulk}^{i-1} - (q_G \cdot A \cdot \Delta t) / (M_{ice} \cdot c_{ice}) \quad (21)$$

230 Since we assume a conical shape with $r_{ice} > h_{ice}$, l_{ice} cannot be greater than $2r_{ice}$ and also cannot
231 be less than Δx . Therefore, the average distance from any point on the surface to any point inside is
232 $\Delta x \leq l_{ice} \leq r_{ice}$. We calculate q_G here assuming $l_{ice} = r_{ice}/2$.

233 3.2.6 Surface temperature changes and melt energy q_{melt}

234 The available net energy q_{net} partly increases surface temperature, but also contributes to ice melt at the
235 surface of the Icestupa. q_T denotes the energy used on changing the surface temperature T_{ice} and q_{melt}
236 denotes the energy used to produce meltwater. So Eqn. 11 can be rewritten as:

$$q_{net} = q_{melt} + q_T \quad (22)$$

237 The temperature fluctuates based on 3 scenarios namely, (1) the energy flux is negative but cannot freeze
238 all the fountain water output; (2) the energy flux is negative and can freeze all the fountain water output and
239 (3) the fountain is inactive ($\Delta M_F = 0$). Also, the latent heat always contributes to temperature fluctuations.
240 Therefore, we express the rate of change of temperature as follows:

$$\frac{\Delta T}{\Delta t} = \begin{cases} -T_{ice}^{i-1} / \Delta t & \text{if } (q_{net} - q_L) < 0 \text{ and } \Delta M_F \geq -(q_{net} - q_L) \cdot A \cdot \Delta t / L_f \\ (\Delta M_F \cdot L_f) / (\rho_{ice} \cdot c_{ice} \cdot \Delta x \cdot A \cdot \Delta t) & \text{if } (q_{net} - q_L) < 0 \text{ and } \Delta M_F < -(q_{net} - q_L) \cdot A \cdot \Delta t / L_f \\ q_{net} / (\rho_{ice} \cdot c_{ice} \cdot \Delta x) & \text{if } \Delta M_F = 0 \end{cases} \quad (23)$$

241 Whenever the model predicts $T_{ice}^{i+1} > 0^\circ C$, then the surface temperature is set to $0^\circ C$ in the corresponding
242 time step and additional energy contributes to q_{melt} . Combining these requirements, we get:

$$(q_T, q_{melt}) = \begin{cases} (\rho_{ice} \cdot c_{ice} \cdot \Delta x \cdot \frac{\Delta T}{\Delta t}, q_{net} - q_L - \rho_{ice} \cdot c_{ice} \cdot \Delta x \cdot \frac{\Delta T}{\Delta t}) & \text{if } T_{ice}^{i+1} \leq 0^\circ C \text{ and } \Delta M_F > 0 \\ (\rho_{ice} \cdot c_{ice} \cdot \Delta x \cdot \frac{\Delta T}{\Delta t}, q_{net} - \rho_{ice} \cdot c_{ice} \cdot \Delta x \cdot \frac{\Delta T}{\Delta t}) & \text{if } T_{ice}^{i+1} \leq 0^\circ C \text{ and } \Delta M_F = 0 \\ (-\rho_{ice} \cdot c_{ice} \cdot \Delta x \cdot \frac{T_{ice}^i}{\Delta t}, q_{net} - q_L + \rho_{ice} \cdot c_{ice} \cdot \Delta x \cdot \frac{T_{ice}^i}{\Delta t}) & \text{if } T_{ice}^{i+1} > 0^\circ C \text{ and } \Delta M_F > 0 \\ (-\rho_{ice} \cdot c_{ice} \cdot \Delta x \cdot \frac{T_{ice}^i}{\Delta t}, q_{net} + \rho_{ice} \cdot c_{ice} \cdot \Delta x \cdot \frac{T_{ice}^i}{\Delta t}) & \text{if } T_{ice}^{i+1} > 0^\circ C \text{ and } \Delta M_F = 0 \end{cases} \quad (24)$$

Table 1. Free parameters in the model categorised as constant, uncertain and site parameters. Base value (B) and uncertainty (U) were taken from the literature. For assumptions (assum.), the uncertainty was chosen to be relatively large (5 %). For measurements (meas.), the uncertainty due to parallax errors is chosen to be (1 %).

Constant Parameters	Symbol	Value	Range	References
Van Karman constant	κ	0.4	n.a.	B: Cuffey and Paterson
Stefan Boltzmann constant	σ	$5.67 \cdot 10^{-8} W m^{-2} K^{-4}$	n.a.	B: Cuffey and Paterson
Air pressure at sea level	$p_{0,a}$	1013 hPa	n.a.	B: Mölg and Hardy
Density of water	ρ_w	$1000 kg m^{-3}$	n.a.	B: Cuffey and Paterson
Density of ice	ρ_{ice}	$917 kg m^{-3}$	n.a.	B: Cuffey and Paterson
Density of air	ρ_a	$1.29 kg m^{-3}$	n.a.	B: Mölg and Hardy
Specific heat of water	c_w	$4186 J kg^{-1} ^\circ C^{-1}$	n.a.	B: Cuffey and Paterson
Specific heat of ice	c_{ice}	$2097 J kg^{-1} ^\circ C^{-1}$	n.a.	B: Cuffey and Paterson
Specific heat of air	c_a	$1010 J kg^{-1} ^\circ C^{-1}$	n.a.	B: Mölg and Hardy
Thermal conductivity of ice	k_{ice}	$2.123 W m^{-1} K^{-1}$	n.a.	B: Bonales et al.
Latent Heat of Sublimation	L_s	$2848 kJ kg^{-1}$	n.a.	B: Cuffey and Paterson
Latent Heat of Evaporation	L_e	$2514 kJ kg^{-1}$	n.a.	B: Cuffey and Paterson
Latent Heat of Fusion	L_f	$334 kJ kg^{-1}$	n.a.	B: Cuffey and Paterson
Gravitational acceleration	g	$9.81 m s^{-2}$	n.a.	B: Cuffey and Paterson
Uncertain Parameters				
Precipitation	T_{rain}	$1 ^\circ C$	$\pm 1 ^\circ C$	B + U: Fujita and Ageta, Zhou et al.
Temperature threshold				
Ice Emissivity	ϵ_{ice}	0.95	$\pm 5 \%$	B: Cuffey and Paterson; U: assum.
Ice Albedo	α_{ice}	0.35	$\pm 5 \%$	B: Cuffey and Paterson; U: assum.
Snow Albedo	α_{snow}	0.85	$\pm 5 \%$	B: Cuffey and Paterson; U: assum.
Albedo Decay Rate	τ	10 days	$[1, 22] days$	B: Schmidt et al.; U: Oerlemans and Knap assum.
Ice layer thickness	Δx	5 mm	$[1, 10] mm$	
Site Parameters				
Fountain diameter	nozzle	dia_F	5 mm	$\pm 1 \%$ B: meas. ; U: assum.
Fountain height		h_F	1.35 m	$\pm 1 \%$ B: meas. ; U: assum.
Fountain temperature	water	T_{water}	$5 ^\circ C$	$[0, 9] ^\circ C$ B: meas. ; U: meas.
AWS height		h_{AWS}	3 m	$\pm 1 \%$ B: meas. ; U: assum.

243 3.3 Mass Balance

$$\frac{\Delta M_{runoff}}{\Delta t} = \frac{\Delta M_F + \Delta M_{ppt} + \Delta M_{dpt} - \Delta M_{ice} - \Delta M_{melt} - \Delta M_{vapour}}{\Delta t} \quad (25)$$

244 where $\Delta M = M^i - M^{i-1}$. Here $\frac{\Delta M_F}{\Delta t} = d_F$ where d_F is the spray of the fountain measured in $[kg s^{-1}]$;
 245 M_{ppt} is the cumulative precipitation and M_{dpt} is the cumulative accumulation through water vapour
 246 condensation or deposition; M_{ice} is the cumulative mass of ice; M_{melt} is the cumulative mass of melt
 247 water; M_{vapour} represents the cumulative water vapor loss by evaporation or sublimation and M_{runoff} is
 248 the cumulative water that drains away.

249 Precipitation input is calculated as:

$$\frac{\Delta M_{ppt}}{\Delta t} = \begin{cases} \pi \cdot r_{ice}^2 \cdot \rho_w \cdot ppt & \text{if } T_a < T_{rain} \\ 0 & \text{if } T_a \geq T_{rain} \end{cases} \quad (26)$$

250 where ρ_w is the density of water ($1000 kg m^{-3}$), ppt is the measured precipitation rate in $[m s^{-1}]$ and
 251 T_{rain} is the temperature threshold below which precipitation falls as snow. Here, snowfall events were
 252 identified using T_{rain} as $1^\circ C$. Snow mass input is calculated by assuming a uniform deposition over the
 253 entire circular footprint of the Icestupa.

254 The latent heat flux is used to estimate either the evaporation and condensation processes or sublimation
 255 and deposition processes. To differentiate between these two possibilities, we classify the time steps into
 256 humid or non-humid if the corresponding relative humidity value is above or below 60 % (Stigter et al.,
 257 2018). On humid time steps we assume condensation or evaporation to occur whereas on non-humid time
 258 steps deposition or sublimation can occur. Correspondingly, latent heat of evaporation (L_e) is used for
 259 humid time steps and latent heat of sublimation (L_s) is used for non-humid time steps. Water accumulation
 260 and vapour loss from the Icestupa surface is calculated as follows:

$$\left(\frac{\Delta M_{vapour}}{\Delta t}, \frac{\Delta M_{dpt}}{\Delta t} \right) = \begin{cases} (-q_L \cdot A/L, 0) & \text{if } q_L < 0 \\ (0, q_L \cdot A/L) & \text{if } q_L \geq 0 \end{cases} \quad (27)$$

261 where $L = \begin{cases} L_e & \text{if } RH \geq 60 \\ L_s & \text{if } RH < 60 \end{cases}$

262 Using the melt energy q_{melt} , we estimate the frozen and melted ice mass (ΔM_{ice} , ΔM_{melt}). Removing
 263 the contribution of precipitation and combining Eqn. 27 we are left with the contribution from the melt
 264 energy as follows:

$$\left(\frac{\Delta M_{ice} - \Delta M_{ppt} - \Delta M_{dpt} + \Delta M_{vapour}}{\Delta t}, \frac{\Delta M_{melt}}{\Delta t} \right) \begin{cases} & \text{if } RH < 60 \\ & \left(\frac{\Delta M_{ice} - \Delta M_{ppt} - \Delta M_{dpt}}{\Delta t}, \frac{\Delta M_{melt} + \Delta M_{vapour}}{\Delta t} \right) \begin{cases} & \text{if } RH \geq 60 \end{cases} \end{cases} = \begin{cases} \frac{q_{melt} \cdot A}{L_f} \cdot (-1, 1) & \text{if } q_{melt} \geq 0 \\ \frac{q_{melt} \cdot A}{L_f} \cdot (-1, 0) & \text{if } q_{melt} < 0 \text{ and } \frac{\Delta M_F}{\Delta t} \geq -q_{melt} \\ \left(\frac{\Delta M_F}{\Delta t}, 0 \right) & \text{if } q_{melt} < 0 \text{ and } 0 \leq \frac{\Delta M_F}{\Delta t} < -q_{melt} \end{cases} \quad (28)$$

Table 2. Summary of calculated mass balance components for the Schwarzsee experiment after the fountain spray was stopped on 15th February 2019 and at the end of the model run on 1st April.

	Mass Component	Fountain spray ends	Model ends
Input	M_F	18060 kg	18060 kg
	M_{ppt}	439 kg	463 kg
	M_{dpt}	14 kg	62 kg
Output	M_{melt}	166 kg	1392 kg
	M_{ice}	1158 kg	0 kg
	M_{vapour} M_{runoff}	4 kg 17184 kg	8 kg 17184 kg

265 Now, with all the other terms known in Eqn. ??, the water runoff from the Icestupa can be expressed as:
 266 Considering AIR as water reservoirs, we can quantify their potential through the amount of water they
 267 store (storage quantity) and the length of time they store it (storage duration). Another means of comparing
 268 different Icestupas is through their water storage efficiency defined accordingly as:

$$\text{Storage Efficiency} = \frac{M_{melt}}{(M_F + M_{ppt} + M_{dpt})} \cdot 100 \quad (29)$$

4 MODEL RESULTS

269 The model was forced with meteorological data from 30th January to 1st April 2019 (Fig. 3) and various
 270 parameters (see Table 1) to calculate the mass and energy balance of the Icestupa.

4.1 Energy and mass balance calculation

272 Daily averages of some components of the energy balance are shown in Fig. 6 (a). On average during the
 273 experiment duration, the total energy flux between the atmosphere and the Icestupa are almost balanced.
 274 Net shortwave radiation (28 W m^{-2}), sensible (17 W m^{-2}) and latent heat flux (9 W m^{-2}) with a mostly
 275 positive flux towards the surface of the icerstupa are compensated by the net longwave radiation (- 36
 276 W m^{-2}) and the melt energy (-19 W m^{-2}). The contribution of other fluxes are negligible in comparison.

277 Net shortwave radiation is the main input to, and the most varying energy flux on the ice surface. Its
 278 variability is controlled by the surface albedo α and the area fraction f_{cone} which therefore represent key
 279 variables in the energy balance (Fig. 7 (a)). Although global radiation flux reached a daily maximum
 280 value of 304 W m^{-2} , q_{SW} only went up to 68 W m^{-2} . This is caused by the fact that only about 30 % of
 281 the direct solar radiation influenced the Icestupa surface as shown by the area fraction f_{cone} in Fig. 7 (a).
 282 Snowfall is the atmospheric variable connected most closely and proportionally to albedo. Higher and/or
 283 more frequent snowfall thus decreases the energy available for melt due to the corresponding increase in α .

284 q_{LW} was predominantly negative indicating that this energy balance component drove the freezing of the
 285 ice structure. The incoming longwave radiation was strongly dependent on atmospheric emissivity which
 286 had a mean value of 0.77. Atmospheric emissivity in turn depended on the cloudiness factor. Daily values
 287 of q_{LW} ranged from -95 to 7 W m^{-2} . q_{LW} and q_S were both proportional to the temperature gradient
 288 between the air and the Icestupa surface. Turbulent sensible heat flux q_S contributed mostly to the melt
 289 of the ice structure. Daily values of q_S ranged from -16 to 59 W m^{-2} . Turbulent latent heat flux q_L was

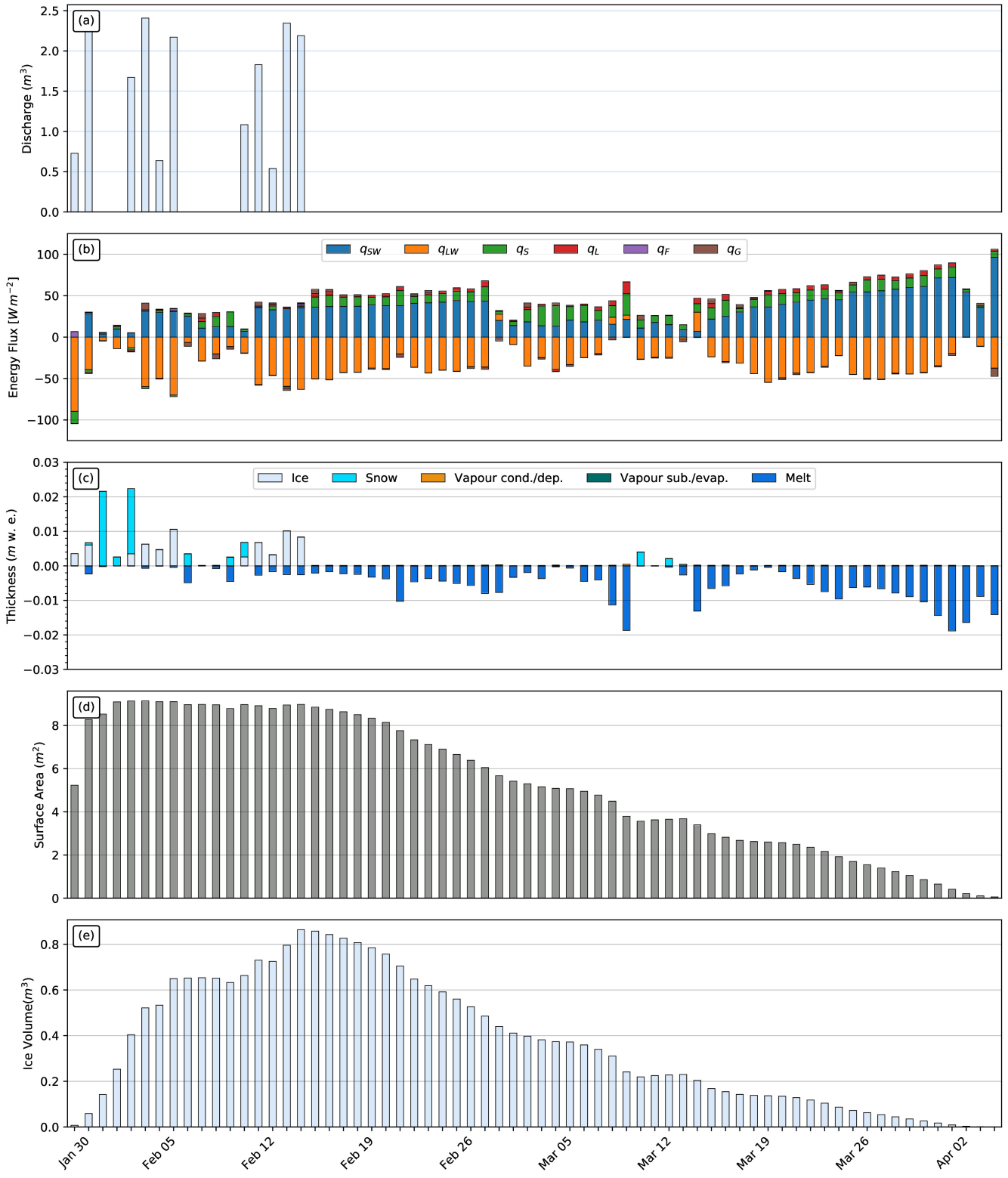


Figure 6. (a) Fountain discharge (b) energy flux components, (c) mass flux components (d) surface area and (e) volume of the Icestupa in daily time steps. q_{SW} is the net shortwave radiation; q_{LW} is the net longwave radiation; q_L and q_S are the turbulent latent and sensible heat fluxes. q_F represents the interactions of the ice-water boundary during fountain on time steps. q_G quantifies the heat conduction process between the Icestupa surface layer and the ice body.

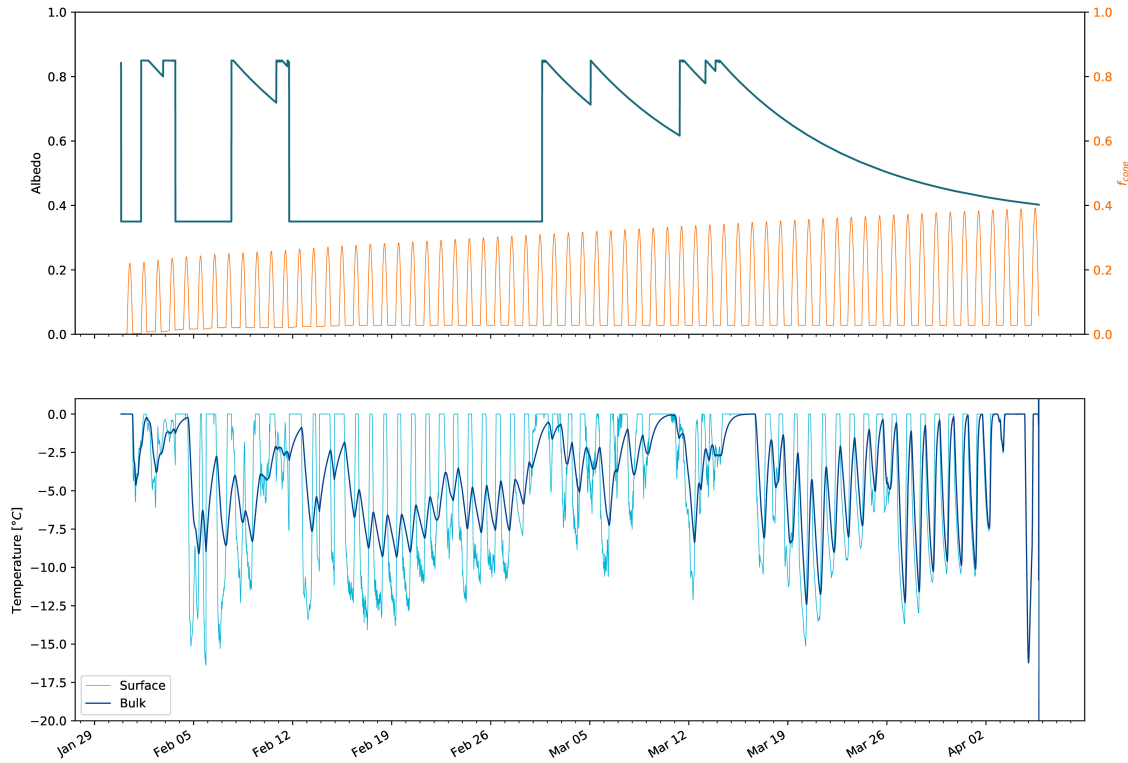


Figure 7. Some derived parameters of the model, namely, albedo and f_{cone} (a), Surface and bulk temperature (b). In (a), the black curve shows how snow and fountain-on events reset albedo between ice albedo and snow albedo. The decay of the snow albedo to ice albedo can also be observed. The blue curve shows how the solar radiation area fraction varied diurnally with variations in the solar elevation angle. In (b), the surface temperature (black curve) was forced to be 0°C during fountain activity. The corresponding bulk temperature is shown with the blue curve.

predominantly positive suggesting that it favoured deposition/condensation over evaporation/sublimation. Daily values of q_L ranged from -4 to 47 W m^{-2} . Therefore, the Icestupa gained mass cumulatively from the atmosphere due to the deposition/condensation process. Fountain water heat flux q_F had a mean of zero as it was only nonzero during 1002 time steps or around 100 hours. Daily values of q_F ranged from 0 to 7 W m^{-2} . The contribution of heat flux by conduction q_G was minimal as it only varied between -7 to 7 W m^{-2} with a mean of 0 W m^{-2} . The energy contributing to surface temperature changes (q_T) was insignificant in comparison to the energy spent on freezing and melting (q_{melt}). The resulting bulk temperature and the surface temperature are shown in Fig. 7 (b). For the total considered period, q_{LW} accounted for 28.3% of overall energy turnover. The energy turnover is calculated as the sum of energy fluxes in absolute values. q_{SW} accounted for 21.7%, followed by q_{melt} (25.4%), q_S (14.6%), q_L (7.5%), q_G (1.8%), q_F (0.3%) and q_T (0.3%).

Fig. 6 (b) represents the mass fluxes associated with these energy exchanges expressed in m w.e. It shows the ice and meltwater formed due to q_{melt} , snow accumulated due to precipitation, water vapour deposition/condensation and sublimation/evaporation due to q_L . Growth rate ($\frac{\Delta M_{ice}}{\Delta t}$) shows a strong correlation with net energy flux ($r^2 = 0.44$) but poor correlation with Icestupa surface area ($r^2 = 0.04$). This is because the variance in growth rate is mostly due to the variance in q_{net} as illustrated in Fig. 6. Since r_{ice} was initialised with the spray radius r_F , the surface area maintains a maximum initially until the

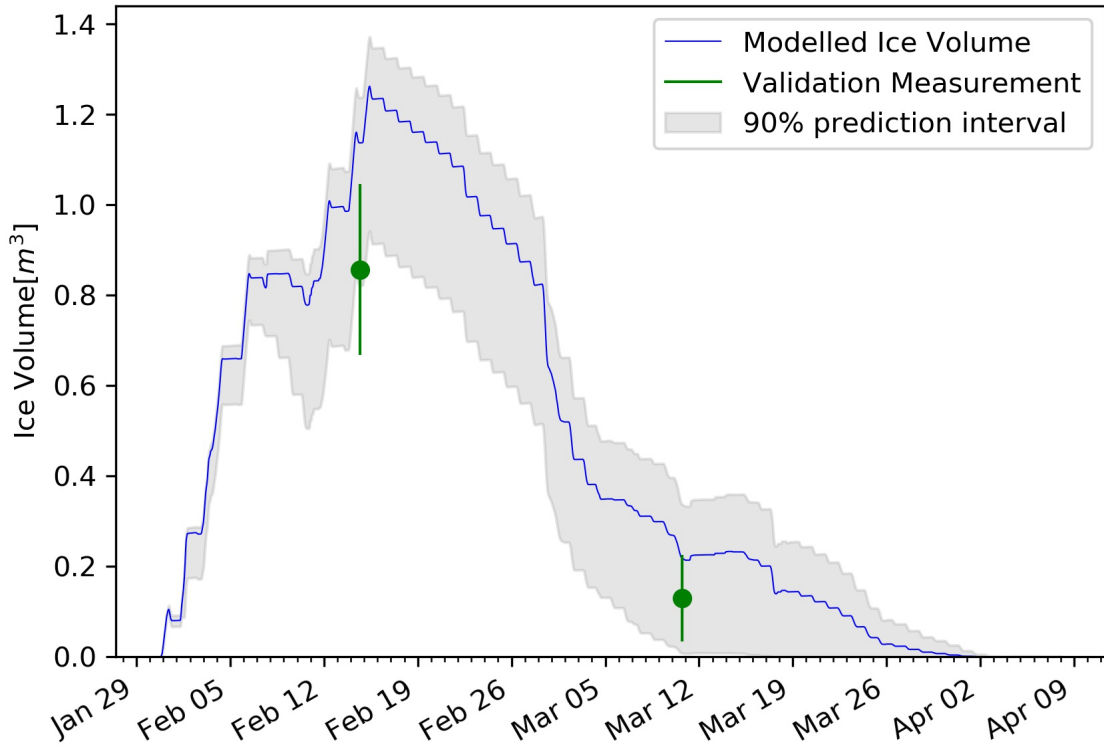


Figure 8. Modelled ice volume during the lifetime of the Schwarzsee Icestupa (blue curve). Green line segments indicate the first and second validation measurements. The prediction interval is based on the ice volume uncertainty caused by the most sensitive parameters, namely, temperature threshold below which precipitation falls as snow and the ice emissivity.

307 energy flux becomes positive. This trend favours the positive over the negative thickness changes resulting
308 in a steep increase and gradual melting of ice volume as can be seen in Fig. 8.

309 The total water used for the Icestupa development includes contributions from the fountain (97.2%),
310 snowfall (2.5 %) and deposition/condensation (0.3 %) as shown in Table 2. The maximum ice mass during
311 the whole measurement period was 1158 kg, which occurred after the last fountain run on Feb 16th in the
312 morning. Therefore, in the case of Schwarzsee we used a water input of 18,584 kg, with a resultant storage
313 efficiency of only 7.5 %.

5 MODEL SENSITIVITY AND UNCERTAINTY ANALYSIS

314 The icestupa model can be regarded as a function $f(x_1, x_2 \dots, x_n) = (y_1, y_2 \dots, y_m)$, where
315 $(x_1, x_2 \dots, x_n)$ are the model parameters and $(y_1, y_2 \dots, y_m)$ are the model outputs. The influence of each
316 parameter on the output variables of interest were quantified and the most important physical parameters
317 for the subsequent uncertainty analysis were determined. The sensitivity of a parameter x_j is determined
318 by keeping all other parameters $x_i, i \neq j$ fixed at their baseline value and varying x_j within values that are
319 physically plausible.

320 A sensitivity study on the parameters (listed in Table 1) was performed with the maximum ice volume
321 as the target variable. All the parameters were assumed to be independent of each other with a uniform
322 distribution. This assumption ignores the auto-correlation present among the parameters associated with
323 the albedo parameterisation. The range of uncertain parameters were set based on available literature values

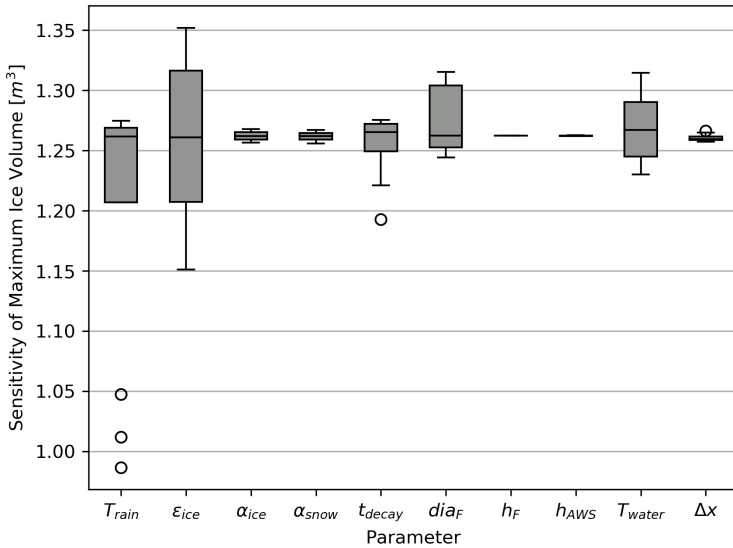


Figure 9. Sensitivities of maximum ice volume to all the uncertain and site parameters used in the model (Table 1). Outliers in the bar plot are shown as 'o'.

324 or varied $\pm 5\%$ from the base value if no such reference was available. The uncertainty of all the site
 325 parameters were caused due to parallax errors during manual measurement. This was quantified with a
 326 range of $\pm 1\%$ from the base value. However, it must be kept in mind that, even though intended to be as
 327 objective as possible, the selection of a parameter range has a subjective part that influences the results and
 328 conclusions obtained in this analysis. The variation of the model outputs y_k is evaluated to quantify the
 329 local sensitivities $s_{j,k}$ that are defined here as the 95% range of the simulated outputs.

330 To perform the uncertainty analysis, we included only parameters that influence the maximum ice volume
 331 by at least $0.1 m^3$. All other parameters were fixed at their baseline value. Fig. 9 shows all the variance
 332 produced by these uncertain parameters in maximum ice volume calculation. It shows that ϵ_{ice} and T_{train}
 333 are the only parameters with a maximal sensitivity of more than $0.1 m^3$ for the maximum ice volume
 334 estimate. Consequently, all other parameters were excluded from the subsequent uncertainty analysis.

335 The temperature threshold below which precipitation falls as snow (T_{train}) was found to be the most
 336 sensitive parameter. It is used in the model to reset the albedo to snow albedo and determine snow
 337 precipitation events. The lower T_{train} parameter the higher the albedo (as the Icestupa surface has a lower
 338 albedo when ice-covered than when snow-covered) . The variation of T_{train} by 5% caused maximum ice
 339 volume variation of $1.2 \pm 0.2 m^3$.

340 Ice emissivity was also found to be a sensitive parameter. The higher the ice emissivity the larger the
 341 maximum ice volume as the emitted longwave radiation increases with ice emissivity. Variation of ϵ_{ice} by
 342 5% caused a maximum ice volume range from $1.3 \pm 0.1 m^3$.

343 In total, the sensitivity analysis required 120 simulations, and the uncertainty analysis a total of 32
 344 simulations.

6 DISCUSSION

345 6.1 Model validation quality

346 We first evaluate the model against the validation measurements at the Schwarzsee site. The uncalibrated
 347 model is able to capture both the freezing and the melting process sufficiently well as the modelled
 348 ice volume lies within the uncertainty of both validation measurements. Furthermore, the validation
 349 measurements fit well within the estimated model uncertainty. However, since this validation is based
 350 on only two points, it does limit the confidence in the model results. Moreover, the model seems to
 351 overestimate the ice volume at both validation points. This could be due to the underestimation of the
 352 surface area which underestimates the melt rates (absolute growth rate when $\frac{\Delta M_F}{\Delta t} < 0$) and the freeze
 353 rates (absolute growth rate when $\frac{\Delta M_F}{\Delta t} > 0$). However, as the fountain was mostly inactive during the study
 354 period, the underestimation of surface area disproportionately undervalues the melt rates over the freeze
 355 rates. One major cause of this underestimation was the conical shape assumption, as in reality, the Icestupa
 356 shape ranged between a cone and a cylinder (Fig. 2). Another cause was the surface irregularities that
 357 were observed due to uneven exposure to direct solar radiation and fountain droplets. The sensitivity of the
 358 model results to these errors was further amplified due to the relatively small volume of the Schwarzsee
 359 Icestupa. In summary, more validation measurements on a more voluminous Icestupa would have increased
 360 confidence on the model results.

361 6.2 Important assumptions

362 In the sensitivity and uncertainty analysis presented above, we did not account for several general
 363 assumptions and parametrisation choices that may cause model errors. Some assumptions and their
 364 potential to cause errors are discussed below.

- 365 • Turbulent Sensible and Latent Heat Fluxes: The method used to calculate the turbulent heat fluxes
 366 by Garratt (1992) assumes that the turbulent heat fluxes are acting over a uniform planar surface to
 367 determine the roughness length. Since our application is on a conical surface, z_{ice} has no real physical
 368 significance.
- 369 • Droplet flight time loss: Water losses during the flight time of fountain droplets were neglected making
 370 all the fountain spray available for freezing. For the Schwarzsee experiment, inclusion of this parameter
 371 does not influence results since it is already accounted for in the runoff water discharge rate which was
 372 at least 3 l min^{-1} .
- 373 • Nucleation of droplets: Corresponding to droplet flight time, ice/snow formation is also possible before
 374 surface contact if nucleation occurs during flight time. For the Schwarzsee experiment, this process
 375 will further increase the freeze rate and hence the storage efficiency. This process is neglected for
 376 model simplicity.

377 6.3 Schwarzsee vs Ladakh Icestupa

378 It could be argued that the relatively small Schwarzsee Icestupa cannot be compared with the much larger
 379 Icestupas in Ladakh which store millions of litres of water for several months (see Appendix 8.1). However,
 380 this is the only Icestupa dataset available for such a model validation.

381 Table 2 clearly shows that for our Schwarzsee experiment most of the input water (92 %) simply runoff
 382 away. This high water loss through drainage is due to the fact that the average spray rate of the fountain
 383 ($(\frac{\Delta M_F}{\Delta t})_{mean} = 3.6 \text{ l min}^{-1}$) far exceeded the max Icestupa growth rate ($(\frac{\Delta M_{ice}}{\Delta t})_{max} = 1 \text{ l min}^{-1}$ (w.e.)).

384 In the city of Leh, Ladakh at an altitude of 3500 m a.s.l. the air temperature shows values down to
 385 27.9°C in winter (Chevuturi et al., 2018) whereas Schwarzsee had a minimum temperature of just -11.6

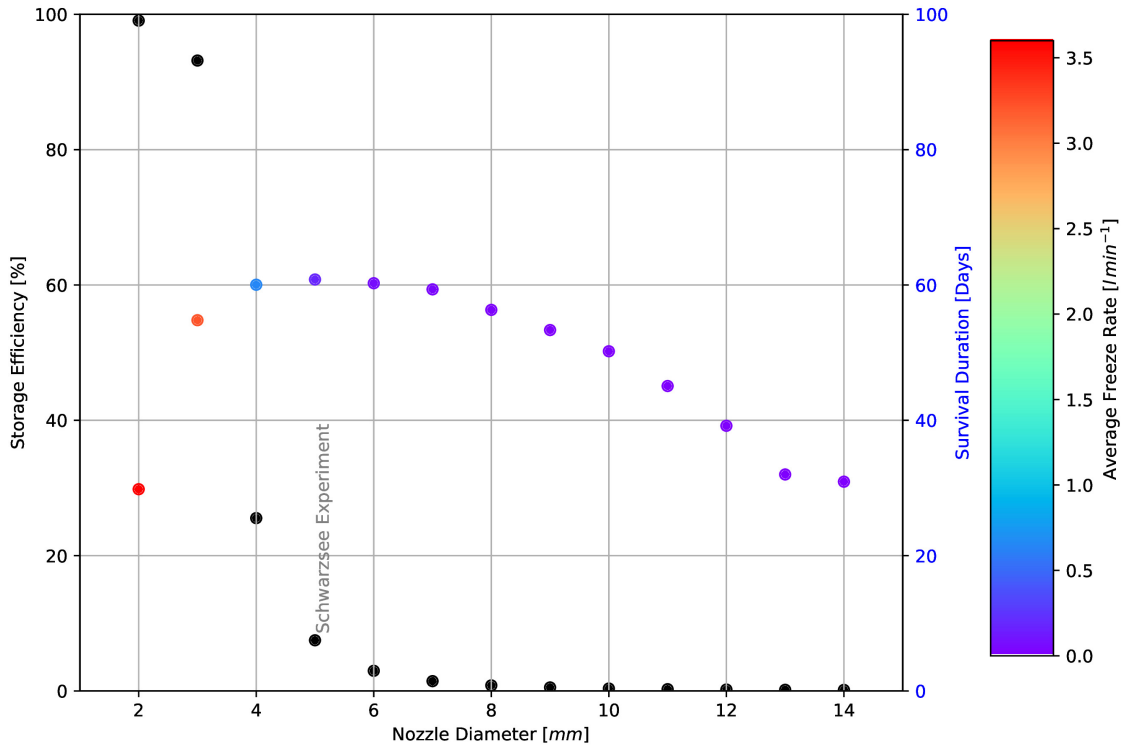


Figure 10. Variation in storage efficiency (black dots) and storage duration (coloured dots) with changes in fountain nozzle's nozzle diameter. The dot colours represent average freeze rate based on the color bar.

386 $^{\circ}\text{C}$ during the study period. Moreover, subzero temperatures were only reached for 7 nights of fountain
 387 operation at the Schwarzsee site compared to the 43 nights of fountain operation possible in Ladakh (see
 388 Appendix 8.1). Thus, the Icestupa growth rate is expected to be much higher in Ladakh. However, water
 389 spray rates in Ladakh are also much higher (around 210 l min^{-1}). So the water losses in Ladakh could
 390 also be caused due to excessive fountain spray.

392 There are several decisions one has to take when constructing Icestupas. These can be broadly divided
 393 into two types of decisions, namely fountain and location decisions. Both the meteorological conditions
 394 of the location and the surface area produced by the fountain significantly influence the observed growth
 395 rate. Since our validation is restricted to just one location, we restrict our discussion to the optimization
 396 possibilities of Icestupa constructions through fountain decisions.

397 Assuming a constant spray for the fountain, we can divide the fountain decisions into fountain state
 398 (on/off) and type (height and nozzle diameter). From an energy balance point of view, the fountain should
 399 be switched on for all time intervals when $q_{\text{net}} < 0$. However, in our experiment, the fountain state decision
 400 was set based on whether the ambient temperature was above or below a critical temperature of -5°C .
 401 Ambient temperature can serve as an indicator of q_{net} as it was correlated ($r^2 = 0.53$). However, q_{net}
 402 was found to be negative already at a critical temperature of -1°C . Therefore, using air temperature to
 403 determine when the fountain should be switched on is justified but a higher critical temperature could have
 404 been used in the case of the Schwarzsee Icestupa.

405 The fountain type used can be characterised by the physical structure of the fountain, namely its height and
406 nozzle diameter. Maintaining the same spray rate and height, one can optimize the Icestupa development
407 by identifying the minimum nozzle diameter that yields the maximum storage efficiency.

408 Fig. 10 shows reducing the nozzle diameter to 3 mm increases storage efficiency up to 93 % without
409 compromising much on storage duration. The corresponding storage quantity of the 3 mm nozzle diameter
410 was more than 20 times higher than the 5 mm fountain used in our experiment. This is because the spray
411 radius r_F of the 3 mm fountain was much higher at 8.5 m compared to the 1.7 m spray radius of the
412 5 mm fountain (see Appendix Section ??). Here, we define growth rate as freeze rate when fountain is
413 active and melt rate otherwise. So this higher spray radius both, increases the freeze rate and increases
414 the melt rate since they are both directly proportional to the surface area. However, since the freeze rate
415 cannot increase beyond a spray rate of 3.6 l min^{-1} (except during precipitation or deposition/condensation
416 events), an optimum spray radius or nozzle diameter exists, beyond which storage duration suffers due to a
417 disproportionate increase in melt rate compared to the freeze rate. So even though 3 mm nozzle diameter
418 had a much higher storage quantity than the 5 mm nozzle, its storage duration was around 6 days less than
419 the 5 mm nozzle. One physical cause of this effect is the different shapes of both the ice structures. A flat
420 sheet of ice (effectively a cone with a high spray radius) with higher mass might have a storage duration
421 shorter than a conical ice structure. As the spray radius decreases with increasing nozzle diameter, the ice
422 structure's average slope increases and so the 5 mm nozzle's ice structure is "more" conical than the 3 mm
423 ice structure. Fig. 10 shows that a nozzle diameter of 3 mm has an average freeze rate ($3.2 \text{ l min}^{-1} \text{ w.e.}$)
424 which is large enough to increase the storage efficiency and small enough to not reduce the storage duration
425 of the Icestupa significantly.

7 CONCLUSIONS

426 We outlined a methodology for estimating ice, liquid water, water vapour and runoff quantities produced
427 during the construction of an Icestupa using measurements of fountain spray rate, air temperature, radiation,
428 humidity, pressure, wind and cloudiness at the Schwarzsee study site. The comparison with validation
429 measurements at two different dates during the experiment led to satisfying results, although a more
430 rigorous model validation was not possible due to few icestupa volume measurements.

431 According to the model, the Schwarzsee Icestupa achieved a storage quantity of 1392 litres of water with
432 a storage duration of 61 days. However, the corresponding storage efficiency was very low with only 7.5 %
433 for a water input of 18,584 litres. These estimates were most sensitive to the temperature threshold that
434 determined precipitation phase and ice emissivity parameters which created an uncertainty of $1.2 \pm 0.3 \text{ m}^3$
435 in the maximum ice volume calculated. This is to be expected as net longwave radiation and net shortwave
436 radiation together accounted for around 50 % of the overall energy turnover.

437 Although the location, storage quantity and duration of our experimental Schwarzsee Icestupa are not
438 representative of the much larger Icestupas of Ladakh, the model results do support the hypothesis that
439 there could be considerable water loss during the formation of Icestupas particularly due to excessive
440 fountain spray. Using model calculations, it was shown that a decreased fountain nozzle diameter of 3 mm
441 can increase the storage efficiency drastically. This is because a change in the fountain nozzle diameter
442 causes an effective change of the ice surface area over which the net energy flux can act. This result has
443 relevance on the future design of Icestupa fountains. However, care has to be taken as our model is currently
444 only validated by one experiment at the Schwarzsee site. Further experiments at different locations with
445 different fountains are required to better understand the influence of construction decisions on the results.

8 APPENDIX

446 8.1 Ladakh Icestupa 2014/15

447 A 20 m tall Icestupa (Wangchuk, 2015c) was built in Phyang village, Ladakh at an altitude of 3500
448 m a.s.l. Assuming a conical shape with a diameter of 20 m, the corresponding volume of this Icestupa
449 becomes 2093 m³ or 1,919,587 litres w.e. The fountain sprayed water at a rate of 210 l min⁻¹ (Wangchuk,
450 2015e) from 21st January (Wangchuk, 2015a) to at least until 5th March 2015 (Wangchuk, 2015b) (around
451 43 nights). Assuming fountain spray was active for 8 hours each night, we estimate water consumption to
452 be around 4,334,400 litres. So just during construction/freezing period of the Icestupa, roughly 56 % of the
453 water provided was wasted. The actual water loss is bound to be much higher due to further vapour losses
454 during the melting period. This Icestupa completely melted away on 6th July 2015 (Wangchuk, 2015d).
455 Therefore, the storage duration was 166 days or roughly 5 months.

CONFLICT OF INTEREST STATEMENT

456 The authors declare that the research was conducted in the absence of any commercial or financial
457 relationships that could be construed as a potential conflict of interest.

AUTHOR CONTRIBUTIONS

458 SB wrote the initial version of the manuscript. MH, ML, SW, JO, and FK commented on the initial
459 manuscript and helped improve it. SB developed the methodology with inputs from MH. SB performed the
460 analysis with support from MH and ML. SB and MH participated in the fieldwork.

FUNDING

461 This work was supported and funded by the University of Fribourg and by the Swiss Government Excellence
462 Scholarship (Suryanarayanan Balasubramanian).

ACKNOWLEDGMENTS

463 We thank Mr. Adolf Kaeser and Mr. Flavio Catillaz at Eispalast Schwarzsee for their active participation
464 in the fieldwork. We would also like to thank Digmesa AG for subsidising their flowmeter used in the
465 experiment. We would particularly like to thank the editor Prof. Thomas Schuler who gave us important
466 inputs to improve the paper and we thank also Prof. Christian Hauck and Prof. Nanna B. Karlsson for
467 valuable suggestions that improved the manuscript.

DATA AVAILABILITY STATEMENT

468 The data and code used to produce results and figures will be published at a later stage and can, until then,
469 be obtained from the authors upon request.

REFERENCES

- 470 Apel, H., Abdykerimova, Z., Agalhanova, M., Baimaganbetov, A., Gavrilenko, N., Gerlitz, L., et al. (2018).
471 Statistical forecast of seasonal discharge in central asia using observational records: development of a
472 generic linear modelling tool for operational water resource management. *Hydrology and Earth System
473 Sciences* 22, 2225–2254. doi:10.5194/hess-22-2225-2018
- 474 Bonales, L. J., Rodriguez, A. C., and Sanz, P. D. (2017). Thermal conductivity of ice prepared under
475 different conditions. *International Journal of Food Properties* 20, 610–619. doi:10.1080/10942912.
476 2017.1306551

- 477 Buck, A. L. (1981). New equations for computing vapor pressure and enhancement factor. *Journal of*
478 *Applied Meteorology and Climatology* 20, 1527 – 1532
- 479 Buytaert, W., Moulds, S., Acosta, L., Bievre, B. D., Olmos, C., Villacis, M., et al. (2017). Glacial melt
480 content of water use in the tropical andes. *Environmental Research Letters* 12, 114014. doi:10.1088/
481 1748-9326/aa926c
- 482 Chen, Y., Li, W., Deng, H., Fang, G., and Li, Z. (2016). Changes in central asia's water tower: Past, present
483 and future. *Nature* doi:10.1088/1748-9326/aa926c
- 484 Chevuturi, A., Dimri, A. P., and Thayyen, R. J. (2018). Climate change over leh (ladakh), india. *Theoretical*
485 *and Applied Climatology* 131, 531–545. doi:10.1007/s00704-016-1989-1
- 486 [Dataset] Copernicus Climate Change Service (C3S) (2017). Era5: Fifth generation of ecmwf atmospheric
487 reanalyses of the global climate
- 488 Cuffey, K. M. and Paterson, W. S. B. (2010). *The Physics Of Glaciers* (Elsevier)
- 489 Fujita, K. and Ageta, Y. (2000). Effect of summer accumulation on glacier mass balance on the
490 tibetan plateau revealed by mass-balance model. *Journal of Glaciology* 46, 244–252. doi:10.3189/
491 172756500781832945
- 492 Garratt, J. R. (1992). *The Atmospheric Boundary Layer* (Cambridge University Press)
- 493 Grossman, D. (2015). As himalayan glaciers melt, two towns face the fallout
- 494 Hersbach, H., Bell, B., Berrisford, P., Hirahara, S., Horányi, A., Muñoz-Sabater, J., et al. (2020). The era5
495 global reanalysis. *Quarterly Journal of the Royal Meteorological Society* 146, 1999–2049
- 496 Hock, R., Rasul, G., Adler, C., Cáceres, B., Gruber, S., Hirabayashi, Y., et al. (2019). 2019: High mountain
497 areas. *IPCC Special Report on the Ocean and Cryosphere in a Changing Climate [H.-O. Pörtner, D.C.*
498 *Roberts, V. Masson-Delmotte, P. Zhai, M. Tignor, E. Poloczanska, K. Mintenbeck, A. Alegria, M. Nicolai,*
499 *A. Okem, J. Petzold, B. Rama, N.M. Weyer (eds.)]*
- 500 Hoelzle, M., Barandun, M., Bolch, T., Fiddes, J., Gafurov, A., Muccione, V., et al. (2019). *The status and*
501 *role of the alpine cryosphere in Central Asia.* doi:10.4324/9780429436475-8
- 502 [Dataset] IDAWEB (2019). Meteoswiss, federal office of meteorology and climatology
- 503 Immerzeel, W. W., Lutz, A. F., Andrade, M., Bahl, A., Biemans, H., Bolch, T., et al. (2019). Importance
504 and vulnerability of the world's water towers. *Nature* 577, 364 – 369. doi:10.1038/s41586-019-1822-y
- 505 Meteoblue (2020). Climate schwarzsee
- 506 Mölg, T. and Hardy, D. R. (2004). Ablation and associated energy balance of a horizontal glacier surface
507 on kilimanjaro. *J. Geophys. Res.-Atmos.* 109, 1–13. doi:10.1029/2003JD004338
- 508 Nüsser, M., Dame, J., Kraus, B., Baghel, R., and Schmidt, S. (2019a). Socio-hydrology of artificial glaciers
509 in ladakh, india: assessing adaptive strategies in a changing cryosphere. *Regional Environmental Change*
510 doi:10.1007/s10113-018-1372-0
- 511 Nüsser, M., Dame, J., Parveen, S., Kraus, B., Baghel, R., and Schmidt, S. (2019b). Cryosphere-Fed
512 Irrigation Networks in the Northwestern Himalaya: Precarious Livelihoods and Adaptation Strategies
513 Under the Impact of Climate Change. *Mountain Research and Development* 39. doi:10.1659/
514 MRD-JOURNAL-D-18-00072.1
- 515 Oerlemans, J. and Knap, W. H. (1998). A 1 year record of global radiation and albedo in the
516 ablation zone of morteratschgletscher, switzerland. *Journal of Glaciology* 44, 231–238. doi:10.
517 3189/S0022143000002574
- 518 Schmidt, L. S., Aðalgeirsdóttir, G., Guðmundsson, S., Langen, P. L., Pálsson, F., Mottram, R., et al. (2017).
519 The importance of accurate glacier albedo for estimates of surface mass balance on vatnajökull: evaluating
520 the surface energy budget in a regional climate model with automatic weather station observations. *The*
521 *Cryosphere* 11, 1665–1684. doi:10.5194/tc-11-1665-2017

- 522 Stigter, E. E., Litt, M., Steiner, J. F., Bonekamp, P. N. J., Shea, J. M., Bierkens, M. F. P., et al. (2018).
523 The importance of snow sublimation on a himalayan glacier. *Frontiers in Earth Science* 6, 108.
524 doi:10.3389/feart.2018.00108
- 525 Tetens, O. (1930). Uber einige meteorologische begriffe. z. *Geophys.* 6, 297–309
- 526 Unger-Shayesteh, K., Vorogushyn, S., Farinotti, D., Gafurov, A., Duethmann, D., Mandychev, A., et al.
527 (2013). What do we know about past changes in the water cycle of central asian headwaters? a review.
528 *Global and Planetary Change* 110, 4 – 25. doi:10.1016/j.gloplacha.2013.02.004. Water in Central Asia
529 – Perspectives under global change
- 530 Wangchuk, S. (2014). Ice stupa artificial glaciers of ladakh
- 531 Wangchuk, S. (2015a). The good news at ice stupa 24th january 2015
- 532 Wangchuk, S. (2015b). Ice stupa artificial glacier inaugurated 5th of march 2015
- 533 Wangchuk, S. (2015c). Ice stupa surpasses guiness world record
- 534 Wangchuk, S. (2015d). Ice stupa way of celebrating a special day
- 535 Wangchuk, S. (2015e). World water day at ice stupa
- 536 WMO (2018). *Guide to Instruments and Methods of Observation* (World Meteorological Organization ;
537 2018 (2018 Edition))
- 538 Woolf, H. M. (1968). *On the Computation of Solar Elevation Angles and the determination of sunrise and*
539 *sunset times* (National Aeronautics and Space Administration)
- 540 Zhou, S., Kang, S., Gao, T., and Zhang, G. (2010). Response of zhadang glacier runoff in nam co basin,
541 tibet, to changes in air temperature and precipitation form. *Chinese Science Bulletin* 55, 2103–2110.
542 doi:10.1007/s11434-010-3290-5